Universiteit
Antwerpen

This item is the archived peer-reviewed author-version of:

Strain analysis from nano-beam electron diffraction : influence of specimen tilt and beam convergence

Reference:
Grieb Tim, Krause Florian F., Schowalter Marco, Zillmann Dennis, Sellin Roman, Müller-Caspary Knut, Mahr Christoph, Mehrtens Thorsten, Bimberg Dieter, Rosenauer Andreas.- Strain analysis from nano-beam electron diffraction : influence of specimen tilt and beam convergence
Ultramicroscopy - ISSN 0304-3991 - 190(2018), p. 45-57
Full text (Publisher's DOI): https://doi.org/10.1016/J.ULTRAMIC.2018.03.013
To cite this reference: https://hdl.handle.net/10067/1514540151162165141

uantwerpen.be
Institutional repository IRUA

Accepted Manuscript

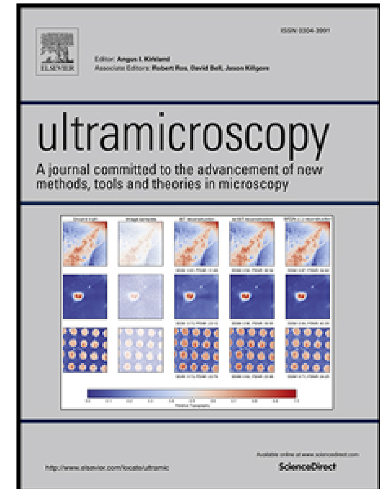

Strain analysis from nano-beam electron diffraction: influence of specimen tilt and beam convergence

Tim Grieb, Florian F. Krause, Marco Schowalter, Dennis Zillmann, R. Sellin, Knut Müller-Caspary, Christoph Mahr, Thorsten Mehrtens, D. Bimberg, Andreas Rosenauer

PII: S0304-3991(17)30513-2
DOI: 10.1016/j.ultramic.2018.03.013
Reference: ULTRAM 12550

To appear in: *Ultramicroscopy*

Received date: 7 December 2017
Revised date: 14 February 2018
Accepted date: 24 March 2018

Please cite this article as: Tim Grieb, Florian F. Krause, Marco Schowalter, Dennis Zillmann, R. Sellin, Knut Müller-Caspary, Christoph Mahr, Thorsten Mehrtens, D. Bimberg, Andreas Rosenauer, Strain analysis from nano-beam electron diffraction: influence of specimen tilt and beam convergence, *Ultramicroscopy* (2018), doi: 10.1016/j.ultramic.2018.03.013

This is a PDF file of an unedited manuscript that has been accepted for publication. As a service to our customers we are providing this early version of the manuscript. The manuscript will undergo copyediting, typesetting, and review of the resulting proof before it is published in its final form. Please note that during the production process errors may be discovered which could affect the content, and all legal disclaimers that apply to the journal pertain.

ACCEPTED MANUSCRIPT

Strain analysis from nano-beam electron diffraction: influence of specimen tilt and beam convergence

Tim Grieb[a,], Florian F. Krause[a], Marco Schowalter[a], Dennis Zillmann[a,b], R. Sellin[c], Knut Müller-Caspary[a,d], Christoph Mahr[a], Thorsten Mehrtens[a], D. Bimberg[c], Andreas Rosenauer[a]

[a]*Institut für Festkörperphysik, Universität Bremen, 28359 Bremen, Germany*
[b]*Institut für Halbleitertechnik, Technische Universität Braunschweig, 38106 Braunschweig, Germany*
[c]*Institut für Festkörperphysik, Technische Universität Berlin, 10623 Berlin, Germany*
[d]*EMAT, University of Antwerp, 2020 Antwerp, Belgium*

ACCEPTED MANUSCRIPT

Abstract

Strain analyses from experimental series of nano-beam electron diffraction (NBED) patterns in scanning transmission electron microscopy are performed for different specimen tilts. Simulations of NBED series are presented for which strain analysis gives results that are in accordance with experiment. This consequently allows to study the relation between measured strain and actual underlying strain. A two-tilt method which can be seen as lowest-order electron beam precession is suggested and experimentally implemented. Strain determination from NBED series with increasing beam convergence is performed in combination with the experimental realization of a probe-forming aperture with a cross inside. It is shown that using standard evaluation techniques, the influence of beam convergence on spatial resolution is lower than the influence of sharp rings around the diffraction disc which occur at interfaces and which are caused by the tails of the intensity distribution of the electron probe.

Keywords: NBED, strain, disc detection, cross aperture, spatial resolution

1. Introduction

Strain in multi-compound semiconductor based devices can either be unfavourable or advantageous - it might limit the incorporation of substituent atoms [1] or it opens new ways to design electronic devices by strain engineering of band gap [2] or carrier mobility [3, 4]. In general, the knowledge of the actual strain state of the specimen is of high importance. Typically, the crystal lattice is strained by a few percent only and changes occur in the (sub) nanometer range. The strain has to be measured with high spatial resolution and with high precision and accuracy for which transmission-electron microscopy (TEM) is a commonly used tool. Strain can be determined e.g. from high-resolution (HR) TEM micrographs (by geometric-phase [5] or peak-pair analysis [6, 7]) or from scanning TEM (STEM) micrographs [8, 9] as well as by the use of holographic techniques [10, 11]. Nanobeam electron diffraction (NBED) allows to measure strain from evaluating the reciprocal distances in series of diffraction patterns [12–19]. As the recording speed of position-sensitive detectors (*cameras*) increased strongly within the last years, strain measurements with high precision and a large field of view were demonstrated for scans in 1 and 2 dimensions [20–26]. The development of NBED *precession* (nanobeam precession electron diffraction [27, 28]) can be seen as a milestone for strain analysis by NBED evaluation.

In all NBED evaluations one or more discs are detected in each pattern of the series by different algorithms and the strain is calculated from the shift of the disc position relative to the position of the undiffracted disc in the center of the NBED pattern. Such a shift of the position of a diffracted disc in reciprocal space corresponds to changes in crystal lattice distances. The interpretation of the measured quantity as *strain* implies the assumption that the measured shift is a direct effect of the change of the lattice parameter in the specimen. One therefore assumes that the *measured* strain represents the *real* strain state of the specimen. A verification of this assumption is difficult to make as in experiment the real strain state of the specimen can only be known with limited accuracy.

In this paper, experimental NBED series for an InGaAs layer embedded in GaAs were recorded for different specimen tilts and strain analyses were performed using disc-detection routines. Multislice simulations of NBED series were performed and it could be demonstrated that strain analysis of these simulated NBED series sufficiently describes the experiment. As the actual strain in the simulation is known, the strain determination from simulated NBED series allows to directly compare the *measured* strain with the underlying *real* strain. With this tool at hand, the influence of tilts on the strain determination is investigated more closely. In addition, modifications from the standard NBED evaluation are suggested in order to minimize the deviation between measured and underlying real strain.

In a separate study the consequences of an increase

ACCEPTED MANUSCRIPT

of the beam-convergence are investigated. Common disc-detection routines as they are suggested in Ref. [16] fail when the discs in the NBED pattern come too close to each other or start to overlap. To overcome this, a structured probe-forming aperture is experimentally realized having a cross inside the usually round aperture. The detection of the crosses in the NBED patterns is possible even for convergence angles which lead to a direct contact of the discs.

In order to investigate whether higher probe convergence can lead to higher spatial resolution in NBED-strain analysis, NBED simulations were performed for an idealized specimen in an additional study. It could be shown that strain profiles across sharp interfaces are broadened mainly due to the so-called *halo* effect suggested in Ref. [29] which will be explained in detail in Sec. 5.2. Using standard evaluation methods, the probe-convergence angle has a smaller influence on the interface broadening compared to the halo effect.

After introducing the experimental and simulation setup in Sec. 2 together with a general description of strain analysis from NBED series, the comparison of experimental and simulated NBED series for different tilts is presented in Sec. 3. A more detailed investigation of the influence of tilt on the measured strain based on simulations is shown in Sec. 4. Sec. 5 deals with the quantitative evaluation of NBED series for increased convergence angles.

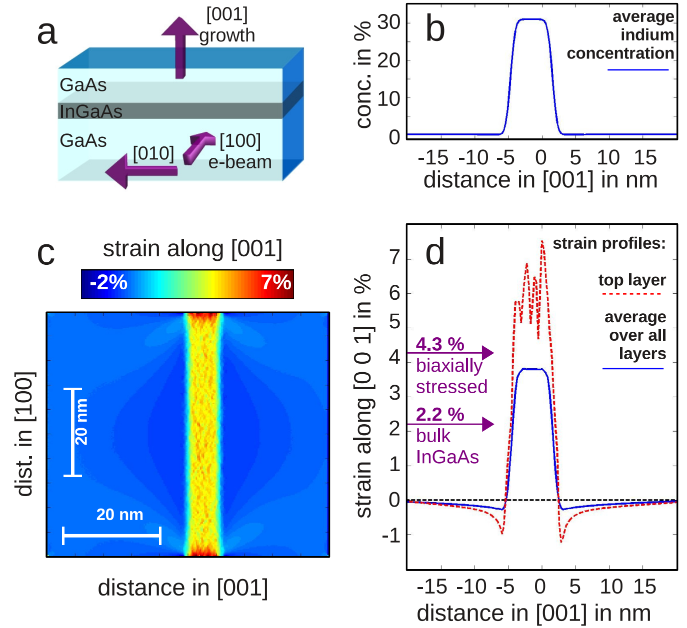

Figure 1: (a) Crystallographic directions for the specimen: the electron-beam direction was always in [100] direction perpendicular to the [001] growth direction. The directions are valid for both, the TEM lamella investigated in the experiment and the super cell used in the simulations. (b) The indium concentration of the super cell used in the simulations along the [001] growth direction averaged along the [010] and the [100] directions (each atomic column along the [010] or [100] direction is nominally homogeneous). (c) Strain ε_{001}^{SC} of the super cell along the [001] growth direction (definition see text) obtained from the atomic positions of the super cell along the [010] direction. ε_{001}^{SC} is shown as a function of position in [001] growth direction and in [100] electron-beam direction. (d) Profiles of the strain of the super cell in [001] growth direction obtained from the 2D strain map in (c): The blue curve shows the strain from averaging over the complete thickness, the red curve the strain state of the top surface layer. Horizontal arrows show the expected strain value for $In_{.31}Ga_{.69}As$ for two cases: unstrained (bulk crystal, lower line) and biaxially stressed (upper line).

2. Experimental and simulation details

Details of the experiment are given in Sec. 2.1 whereas the analysis of the indium concentration and the specimen thickness of the investigated specimen can be found in the Appendix A. Based on the experimental parameters, simulations are set up which are described in Sec. 2.2. The standard procedure how to measure strain from NBED series is described in Sec. 2.3.

2.1. Experimental details

The investigated sample was an InGaAs layer embedded in GaAs grown by metal-organic chemical vapour deposition (MOCVD [30, 31]) along the [001] direction. The indium concentration in the InGaAs layer was 31 % indium measured using quantitative high-angle annular dark field (HAADF) STEM (details can be found in the Appendix A). A TEM lamella with [100] electron-beam direction in TEM was prepared by lift-out using an FEI Nova Nanolab 200 focused-ion beam (FIB). The crystallographic directions are schematically shown in Fig. 1a. Low-voltage ion milling was applied afterwards using a Technoorg Linda IV5 at 400 V acceleration voltage [32, 33]. Before TEM measurements, the sample was plasma cleaned using a Binder TPS 216 plasma cleaner operated with Ar/O plasma. TEM analyses were performed with a Titan 80/300 microscope at 300 kV acceleration voltage. For quantitative HAADF STEM a Fischione 3000 detector was used. Position-averaged convergent-beam electron diffraction (PACBED [34]) was used to measure the specimen thickness at the positions where the NBED series were recorded and results in 54±2 nm (details of this measurement can also be found in the Appendix A). PACBED images and NBED-image series were recorded with a Gatan UltraScan 1000 CCD camera with applied energy filtering using a Gatan imaging filter (GIF).

2.2. Simulation Details

NBED simulations for a GaAs super cell with an InGaAs layer in the center along the [001] growth direction were performed using the absorptive-potential multislice approach [35, 36] in the STEMsim program [37]. The super cell used had dimensions of 100 unit cells in [001] direction and 50 unit cells in [010] direction and 50 pixels per unit cell, both in [001] and [010] direction. The distance between the central disc and the 004 disc in the simulated NBED patterns was approximately 200 px - this value was not varied in the presented simulations. An InGaAs layer

in the center of the super cell was created by replacing Ga by In atoms with a maximum concentration of 31 % in accordance with the HAADF-STEM results. The indium-concentration profile of the embedded InGaAs layers is shown in Fig. 1b. The super cell was relaxed using valence-force field calculations with the LAMMPS code [38, 39] causing static-atomic displacements (SADs) [40–42] as well as surface-strain relaxation [43–45]. The strain with the definition $\varepsilon_{001}^{SC} = \frac{d-d_{GaAs}}{d_{GaAs}}$ along the [001] growth direction was derived from the atomic distances d of the relaxed super cell (with d_{GaAs} being the distance at the border of the super cell). The strain ε_{001}^{SC} averaged in [010] direction is visualized in Fig. 1c as a function of the position in [001] growth direction as well as the position in [100] electron-beam direction. Visible fluctuations in the highly strained central layer are caused by SADs. The blue profile in Fig. 1d shows the strain along the [001] growth direction averaged over the complete thickness of the super cell. The maximum strain in the central InGaAs layer is higher compared to the value which would be obtained from InGaAs bulk material (lower horizontal arrow in Fig. 1d) and smaller compared to the strain observed for the biaxial strain state corresponding to an infinitely thick specimen. (upper horizontal arrow in Fig. 1d). The reason is that the elastic relaxation of the super cell partially reduces the tetragonal distortion of the InGaAs lattice.

In the simulations, different beam tilts were applied to the same super cell which is equivalent to sample tilt. An NBED line scan in the simulation was performed by scanning over the central 80 unit cells along the [001] direction with 3 scan points per unit cell. For each scan point the NBED pattern was stored after a specimen thickness of 55 nm to make the simulation comparable to the experimental measurements. The thickness was the same for all simulations in this study.

It was shown in a previous study [46] for individual undiffracted NBED discs that experimental effects have to be considered in the simulation in order to achieve results for disc detection which are comparable to experiment. Such effects are Poisson noise and the recording process by a CCD camera. The following consideration is explained in detail in Ref. [46]. The intensity in the background of the discs within the energy-filtered experimental NBED pattern is rather constant. Thus, a constant background of 300 counts is added to the simulation and the average disc intensity of the central disc is scaled to a value of approximately 4000 counts. In experiment, the sharp borders of the discs are blurred by the recording process with the pixelated CCD camera with a scintillator on top. This effect was taken into account by considering the modulation-transfer function (MTF) [47] of the used CCD camera. The MTF was obtained experimentally as described in Ref. [47, 48]. The Poisson distribution of the incoming electrons as well as additional noise in the experimental image is taken into account by randomly distributing N_e electrons with the probability given by the raw simulation, where N_e is chosen so that the noise characteristics of experiment and simulated images are similar [46]. The individual steps are performed in the following order: 1. Distributing electrons to simulate noise, 2. applying the MTF to take the recording system into account, 3. adding background and scaling the disc intensity.

2.3. Measuring strain from NBED series

The strain was calculated for simulated and experimental NBED profiles in the same way. Each NBED image contained the central 000 disc as well as the 004 disc. If not stated differently in the text, only the strain in [001] growth direction was calculated by evaluating the disc positions of the 000 and the 004 discs. For both discs, position and radius were set manually and refined from a single image using the radial-gradient maximization algorithm as suggested in Ref. [16]. Then, the radius was kept constant and the disc positions were fitted for the complete series using the same detection algorithm or the cross-correlation method [16]. The ***strain*** ε_{001} in growth direction was calculated by [16]

$$\varepsilon_{001} = \frac{R_{004}}{R_{004} + \Delta_{004}} - 1 \tag{1}$$

with R_{004} being the distance between the central disc and the 004 disc within an (unstrained) GaAs region and Δ_{004} being the deviation from this value caused by the change of the lattice parameter in strained regions. This analysis was suggested in Ref. [16] denoted as ***SANBED*** for *strain-analysis by nano-beam electron diffraction.* This abbreviation is kept in this paper as long as no modifications to the originally suggested method are made.

In the presented study, strain is evaluated for different parameters, such as the applied specimen tilt. To compare strain profiles of different series, the ***precision*** is measured from each profile as done e.g. in Ref. [29]: The precision is defined as the standard deviation obtained from the first 30 to 50 points in the strain profile (which lie in a region of nominally unstrained GaAs) from which a low-order polynomial fit was subtracted. This subtraction was performed to only consider short-range variations of the measured strain.

3. Simulation of NBED series for strain analysis

In Sec. 3.1, experimental NBED series are compared to simulated ones in terms of strain analysis using the SANBED method. The results suggest that the strain analysis from simulation is able to reproduce characteristic details within the experimental strain profiles. In Sec. 3.2 the strain measured from these simulated NBED series is compared with the known underlying strain used as input.

3.1. Comparison of experiment and simulation

An experimental tilt series of six different specimen tilts was performed and for each tilt, six NBED series were recorded, not from the same specimen position but

ACCEPTED MANUSCRIPT

ACCEPTED MANUSCRIPT

all stemming from regions very close to each other. The applied semi-convergence angle was 2.6 mrad. The specimen tilt is characterized by two angles, b and c, measuring the rotation between the incident beam direction and the [100] direction. These two angles gives the location of the center of Laue circle (a; b; c) with $a = 0$. Four tilts were applied primarily in [001] growth direction with values for b and c of: (1) ($b = \overline{0.4}$; $c = 0.2$), (2) ($b = 0$; $c = 1.2$), (3) ($b = 0$; $c = 1.6$) and (4) ($b = 0$; $c = 3.1$). Additionally, two relatively large tilts were applied perpendicular to the growth direction: (5) ($b = 10.5$; $c = 1.5$) and (6) ($b = 16$; $c = 1.5$).

The strain along the [001] growth direction was determined by the SANBED method as described in Sec. 2.3 using the radial-gradient maximization method [16]. The black curves in each subfigure in Fig. 2 show the six experimental strain profiles for the given specimen tilt. From the profiles for tilt (1) in Fig. 2a it becomes obvious that in the GaAs regions the measured strain is not constant but shows fluctuations with regions of positive strain (*hills*) and those with negative strain (*dips*). Whereas some features change over the six scans (as those marked with R1 in Fig. 2a), others appear characteristically in all scans, such as the strain dips next to the InGaAs layer, marked with R2. The changing features might be explained by slightly different orientations at the six scan positions. But the characteristic features seem to be connected with the distinct properties of the investigated sample, the imaging conditions (including the sample tilt) and the evaluation conditions (disc-detection procedure and possibly choice of evaluated disc).

For the tilts (2-4) in Fig. 2b-d, the 004 disc is generally more excited so that the deviations between the single scans are smaller, as the precision for detecting the disc is better. The following characteristic features obviously change for the different tilts: 1. the *appearance of strain dips* next to the InGaAs layer, 2. the *difference in the average strain level* on the left and the right-hand side of the InGaAs layer (for tilt (1), the strain on the right-hand side is lower, for tilt (4) it is vice versa) and 3. the *maximum strain* in the InGaAs layer (which is approximately 4 % except for tilt (1) where it is significantly lower). Figs. 2e and f show comparable profiles for the two tilts (5) and (6) which are characterized by a high tilt angle b. These profiles are very similar to each other but clearly differ from those in Fig. 2a. This shows that a high tilt ($b = 10 - 16$) perpendicular to the growth direction reduces the appearance of strain features but the shape of the profile is less sensitive to the amount of tilt.

The red and blue curves in Figs. 2a-f show the strain profiles from evaluating the simulated NBED series. Simulations were performed as described in Sec. 2.2 and both, disc detection and strain determination, were applied identically to those for the experimental series. The indium distribution and the strain in the simulation were chosen to describe the experiment as well as possible. Nevertheless, a perfect agreement between simulation and experiment

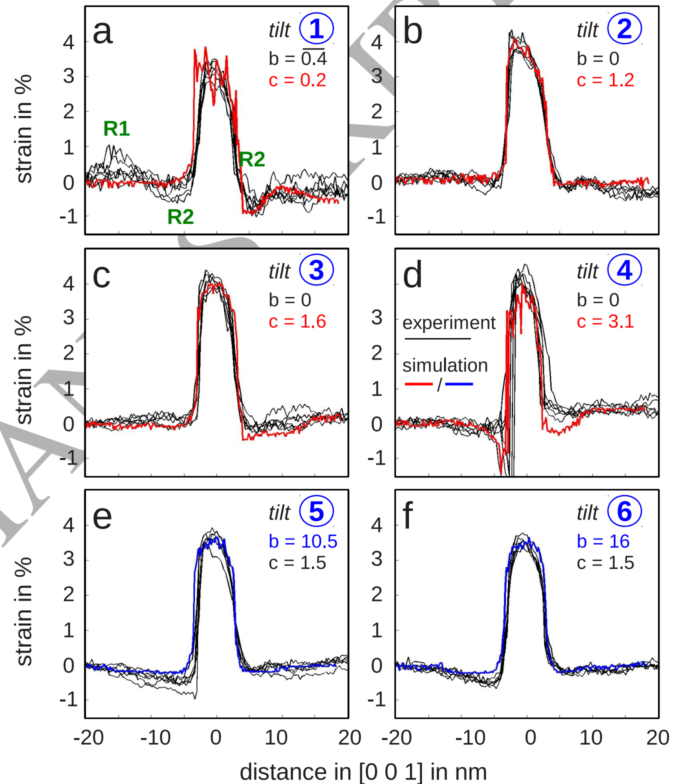

Figure 2: (a-f) Strain profiles from the analysis of the position shift of the 004-NBED disc for six different specimen tilts (1-6) characterized by the center of Laue circle (a; b; c). With $a = 0$, the tilts can be described by following tilt angles: (1) ($b = \overline{0.4}$; $c = 0.2$), (2) ($b = 0$; $c = 1.2$), (3) ($b = 0$; $c = 1.6$), (4) ($b = 0$; $c = 3.1$), (5) ($b = 10.5$; $c = 1.5$) and (6) ($b = 16$; $c = 1.5$). The legend shown in (d) is valid for (a-f): Black curves show experimental data (six scans), coloured curves show the corresponding data from simulations.

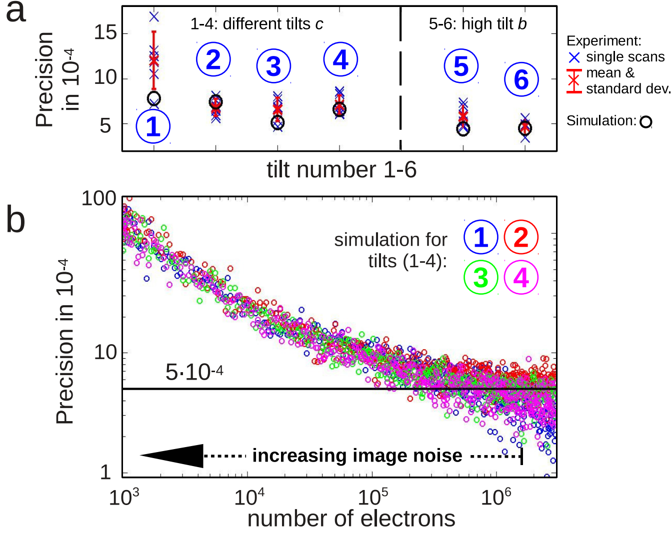

Figure 3: (a) Precision of the strain profiles from Fig. 2 for experiment (blue crosses) and simulation (circles). The red crosses show the mean values of all experimental scans for for an individual tilt (1-6), the red error bars show the standard deviations. (b) Double-logarithmic plot of the precision of simulated strain profiles for different noise levels. The four colors indicate the tilts (1-4). The horizontal line is placed at a precision of $5{\cdot}10^{-4}$.

cannot be expected as the experimental conditions and sample properties depend on many parameters and might change even between two scans. However, also in the simulation the characteristic features which appeared in experiment are visible: 1. The appearance of strain dips next to the InGaAs layer are at least similar to those from experiment. 2. The difference in the average strain level is qualitatively comparable to the experiment. 3. Also in the simulation, the maximum strain within the InGaAs layer is reduced for tilt (1). The tilt (4) with c = 3.1 in growth direction leads to a weak excitation of the 004 disc. This affects the strain detection in experiment as well as in the simulation as it becomes obvious from the large errors close to the interface at the left-hand side (Fig. 2d).

Fig. 3a shows the precision of the strain as defined in Sec. 2.3 for the simulations (circles) and the experimental scans (blue crosses; the red crosses show the mean values over all scans for a certain tilt (1-6), red error bars the corresponding standard deviations). Within the variation of the single scans, the precision for all tilts is in the range of 6-12$\cdot10^{-4}$. Obviously, tilting the sample perpendicular to the [001] growth direction (tilts (5) and (6)) leads to a better precision. Here, the 004 disc is more homogeneously illuminated since the dynamic electron interaction with reflections outside of the systematic row is reduced. The precision is comparable to values found in literature - there, precision is calculated to 7-9$\cdot10^{-4}$ for experimental SANBED [16] and 9-13$\cdot10^{-4}$ for simulations of SANBED [29]. Values for strain precision for other NBED techniques of 10$\cdot10^{-4}$ [49], 7.5$\cdot10^{-4}$ [50] and 6$\cdot10^{-4}$ [14] are published. For comparison, *precession* NBED reaches a precision of 2-5$\cdot10^{-4}$ [51].

Of course, precision depends on the amount of noise applied to the simulation. Fig. 3b shows the calculated strain precision for the simulated NBED series where the strain determination was performed for different numbers of electrons N_e, resulting in various Poisson-noise levels. For very low N_e, starting at 1000 electrons, the discs are hardly detected resulting in poor precision - with values up to 100$\cdot10^{-4}$. But with increasing N_e, the precision value exponentially decreases to approximately 5$\cdot10^{-4}$ for N_e =10^6 electrons. For higher N_e, the precision is improving only slowly.

In conclusion, the presented simulations of NBED series do not describe the experiment in every detail but show strain characteristics as they occur in experiment. The strain profiles behave similar in terms of tilting and show a comparable precision. Consequently, it can be assumed that the important properties which lead to characteristic strain features in experiment are described by the used simulations. Therefore, simulations can be used in the following to directly compare the strain profiles measured from NBED series with the *real strain* which is underlying in the simulation.

3.2. Measured strain vs. actual strain

Fig. 1c shows the actual strain along the [001] growth direction of the super cell. The atomic layers which are close to the bottom and top surfaces show a higher strain along the [001] direction as also relaxation in [100] electron-beam direction occurs (surface-strain relaxation, e.g. see Ref. [44]). Fig. 1d shows strain profiles from averaging the strain in Fig. 1c along the [100] electron-beam direction over the complete super cell (blue) as well as the strain profile of just the first layer (red). As the strain is not homogeneous along the beam path, it is important to know whether the SANBED method gives a strain profile which is in acceptable agreement with the true profile averaged along the electron-beam direction: The comparison of the strain profiles derived from simulated NBED series in Fig. 2 with the actual strain profiles from the super cell in Fig. 1d suggests that a maximum strain in the InGaAs layer is measured which is comparable to the average strain over the complete thickness of the super cell (blue curve in Fig. 1d). This result is in agreement with results from a previous study on nanoporous gold [52]. Consequently, in the following comparisons the measured strain is always compared to the strain averaged over the super cell which is denoted as *real strain.*

4. Influence of tilt on the measured strain

In Sec. 3.1 it was shown that different beam tilts lead to different shapes of the strain profile with strain features - such as dips - occurring with different strength. For further investigation simulations are compared for different tilts: For a tilt series in [001] growth direction in Sec 4.1 and for a

ACCEPTED MANUSCRIPT

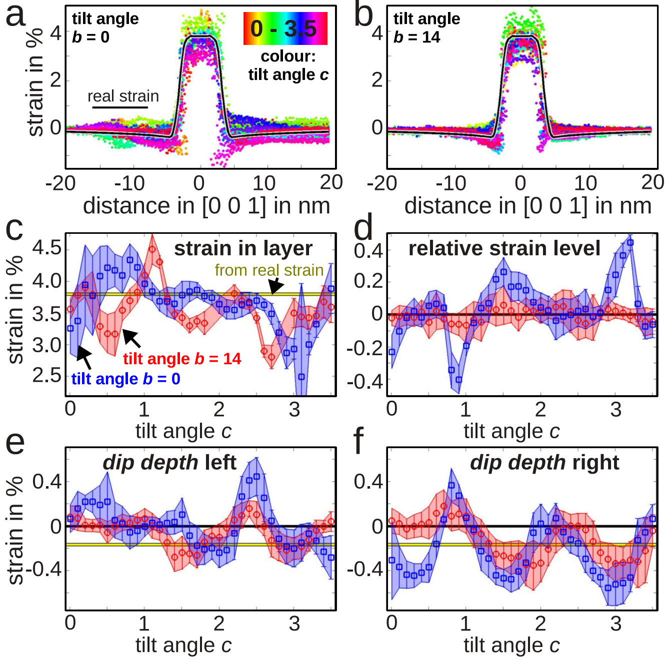

Figure 4: Strain from simulated NBED series for a tilt series in [001] growth direction defined by the tilt angle c. (a,b) Strain profiles for different values of c are represented by different lines colors. In (a) no additional tilt perpendicular to growth direction was applied ($b = 0$), in (b) a tilt angle of $b = 14$ was set. Solid black profile shows real strain. (c-f) Profile characteristics vs. tilt angle c in [001] direction for $b = 0$ (blue) and for $b = 14$ (red): (c) Strain in the InGaAs layer, (d) difference in strain level between left and right GaAs region, (e) strain difference between region on the left-hand side of the InGaAs layer to the substrate, (f)strain difference between region on the right-hand side of the InGaAs layer to the substrate. Error bars show standard deviation. The yellow horizontal line in (c,e,f) shows expected value from real strain.

constant absolute tilt pointing towards different directions in Sec. 4.2.

4.1. Influence of tilt: Inclination angle

Simulations of NBED series comparable to those from Sec. 3.1 were performed for various tilts in [001] growth direction. Resulting strain profiles are shown in Fig. 4a and b where each profile (color) shows the strain for a different tilt expressed by the value of the third component of the applied center of Laue circle $0 \leq c \leq 3.5$. The tilt perpendicular to the growth direction was $b = 0$ in case of Fig. 4a and $b = 14$ in case of Fig. 4b. Fig. 4c shows the average measured strain in the center of the InGaAs layer as a function of the applied c for the two cases, $b = 0$ (blue) and for $b = 14$ (red), respectively. Error bars show the standard deviation from averaging the strain in the InGaAs layer. At scan points for tilt angles c which hardly excite the investigated 004 disc (low tilt angles $0 \leq c \leq 0.6$ and high tilt angles $3 \leq c \leq 3.5$) the intensity distribution in the 004 disc was in some cases not sufficient for disc detection. Those data points - only approximately 1 % of the total number of data points - where excluded from the profiles. In consequence, very large error bars such as for $c = 3.1$ in Fig. 4c are caused by the low number of valid scan points. Obviously, the average strain fluctuates around the real-strain value of approximately 3.8 % (horizontal yellow line).

The smallest deviation to this nominal strain for $b = 0$ is choosing c approximately between 1 and 2.5. Fig. 4d shows the difference between the strain level within the GaAs region at the right end of the profile to the strain level at the left end of the profile. For $b = 14$ differences in the strain levels do not occur. For $b = 0$ differences in the strain levels can be positive or negative dependent on the value of c. Figs. 4e and f show the *dip depth* which is the strain difference between the GaAs region close the InGaAs layer and the GaAs region far away from the layer. Fig. 4e shows this difference for the regions on the left-hand side of the InGaAs layer and Fig. 4f for those on the right-hand side. The horizontal yellow line shows the expected value from the real strain - which is not zero but slightly negative. It seems that the strength of the increase or decrease of strain changes periodically with c where a negative value (*dip*) appears more often than a positive one (*hill*). The results suggest that the shape of the profile - and consequently deviations to the actual underlying strain - strongly depend on the applied tilt. For the simulated case, a good agreement to the real strain would be obtained for $c \approx 1.8$. It is important to note that the suggested tilt is valid in case of the used specimen thickness. It may vary for thicker or thinner specimen.

4.2. Influence of tilt: Azimuthal angle

Simulations of an NBED series were set up with a defined absolute tilt of 7 mrad pointing towards different directions: the tilt is precessing around 360° in 32 equidistant steps resulting in 32 NBED patterns for each scan point of the series.

Figure 5a shows two strain profiles from evaluating the 004 disc and $00\bar{4}$ disc for a tilt perpendicular to the [001] growth direction. One NBED pattern from the series is exemplarily shown in Figure 5a with the tilt visualized by an arrow ($b \approx 2$, $c = 0$). The strain level on the right-hand side of the InGaAs layer is slightly negative for the evaluation of the 004 disc (red profile) and positive in case of the $00\bar{4}$ disc (blue profile). The green profile shows the real strain in all Figures 5a-c.

Figure 5b again shows the strain profiles from evaluating the 004 and the $00\bar{4}$ discs but now from two NBED patterns. For each NBED pattern, an individual tilt was applied which strongly excites the $00\bar{4}$ disc ($b = 0$, $c \approx \bar{2}$) or the 004 disc ($b = 0$, $c \approx 2$), respectively. Here, the strain features appear mirrored: the strain *dip* on the left-hand side of the InGaAs layer in the red profile (004 disc) appears on the right-hand side in the blue profile ($00\bar{4}$ disc).

Fig. 5c shows strain profiles originating from a different way of evaluation: the strain was calculated from the distance between the 004 and $00\bar{4}$ discs (*opposite-discs evaluation*) instead of the distance between the 004 (or

ACCEPTED MANUSCRIPT

ACCEPTED MANUSCRIPT

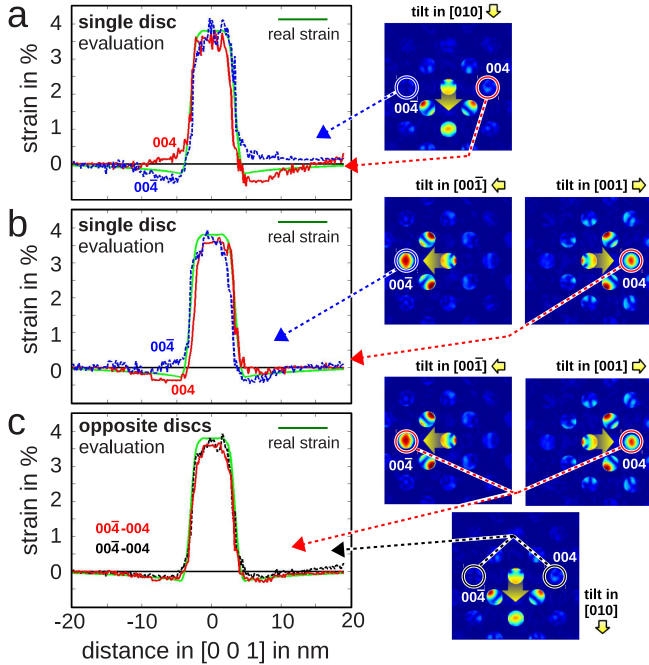

Figure 5: Strain profiles for tilts of 7 mrad pointing towards different directions. The green profile shows the real strain in (a-c). Other profiles show strain from evaluating discs marked by circles in the NBED patterns. (a) Both curves (red and blue) stem from a single image series with a tilt in [010] direction ($b \approx 2$, $c = 0$, *single-disc evaluation*). (b) Each curve was evaluated from an individual image series where the tilt was chosen to strongly excite the evaluated disc ($b = 0$, $c \approx \bar{2}$ (blue), $c \approx 2$ (red), *single-disc evaluation*). (c) The red curve stems from *opposite-discs evaluation* where each disc was taken from an individual image series with a tilt that strongly excites the evaluated disc ($b = 0$, $c \approx \bar{2}$ (series 1), $c \approx 2$ (series 2)). The black curve corresponds to *opposite-discs evaluation* from a single image series with a tilt in [010] direction ($b \approx 2$, $c = 0$).

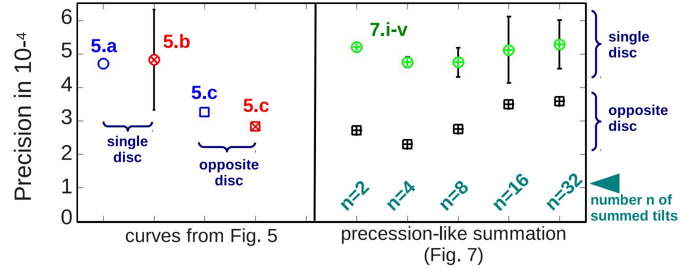

Figure 6: The strain precision for the profiles in Fig. 5 (left) and Fig. 7 (right) where the figure number is given next to each data point. Colour representation: Tilts that strongly ($|c| = 2$, red) or weakly ($c = 0$, blue) excite the evaluated disc in Fig. 5. Green and black curves show precession-like summation of many tilts for different n. Marker type: data from single-disc (circles) or from opposite-discs (squares) evaluation. In Fig. 7 only the profiles corresponding to single-disc evaluation are shown.

00$\bar{4}$) disc and the center of the NBED pattern (*single-disc evaluation*). The red profile in Fig. 5c shows the evaluation for strongly excited 004 and 00$\bar{4}$ discs from two individual NBED patterns: the position of the 00$\bar{4}$ disc was determined from a series with $b = 0$ and $c \approx \bar{2}$, the position of the 004 disc from a series with $b = 0$ and $c \approx 2$. The black profile shows the strain from evaluating the same opposite discs but for a single NBED pattern without a tilt in [001] growth direction ($b \approx 2$ and $c = 0$). Both profiles show less strain features compared to the single-disc evaluation in Fig. 5a and b. The comparison of the red and the black curve in Fig. 5c shows that the evaluation from two images, both tilted towards opposite directions ($|c| = 2$) does not lead to a significant broadening of the strain profile compared to the case for $c = 0$.

The left part of Fig. 6 shows the precision of the measured strain from the considered profiles where the number next to each data point corresponds to the profile in Fig. 5a-c from which the precision is calculated. For the single-disc evaluation the upper and lower end of the black error bars show the individual evaluations for the 004 and the 00$\bar{4}$ disc, the data points show the average value. The precision is not significantly better for the case of the strongly excited disc (red) with $|c| = 2$ compared to the weakly excited disc (blue) with $c = 0$ in this simulation. The precision for opposite-discs evaluation (square symbols) is improved with respect to single-disc evaluation (circles).

In the following, NBED patterns are formed by summation of different numbers of simulated NBED patterns for different azimuthal tilts. The presented simulation for InGaAs is similar to the one published in Ref. [29] for silicon in [110] electron-beam direction where image noise was ignored. The black curves in Fig. 7 show strain profiles from evaluating the 004 disc from NBED patterns, each created by the sum of n differently tilted NBED patterns ($n = [2, 4, 8, 16, 32]$). For each summation, the n tilts were always equidistant and the tilts in [001] and in [00$\bar{1}$]

ACCEPTED MANUSCRIPT

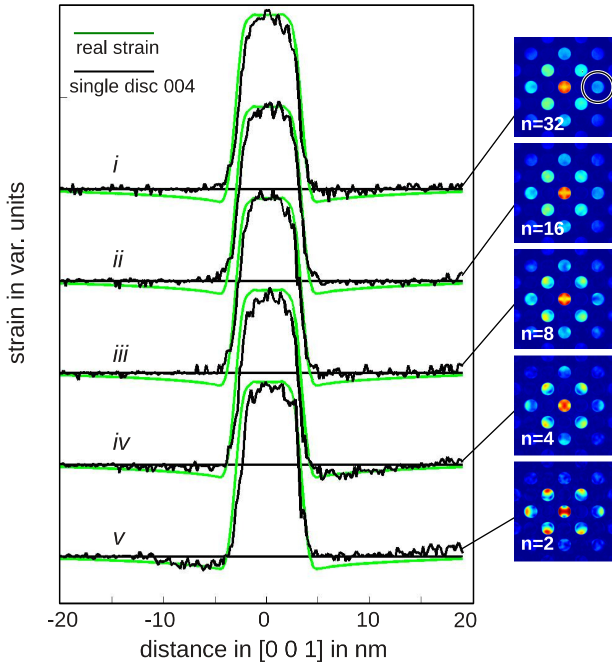

Figure 7: Black curves show strain profiles from single-disc evaluation of *precession-like* summation of n equidistant tilts (see text for explanation). The green profiles show the real strain.

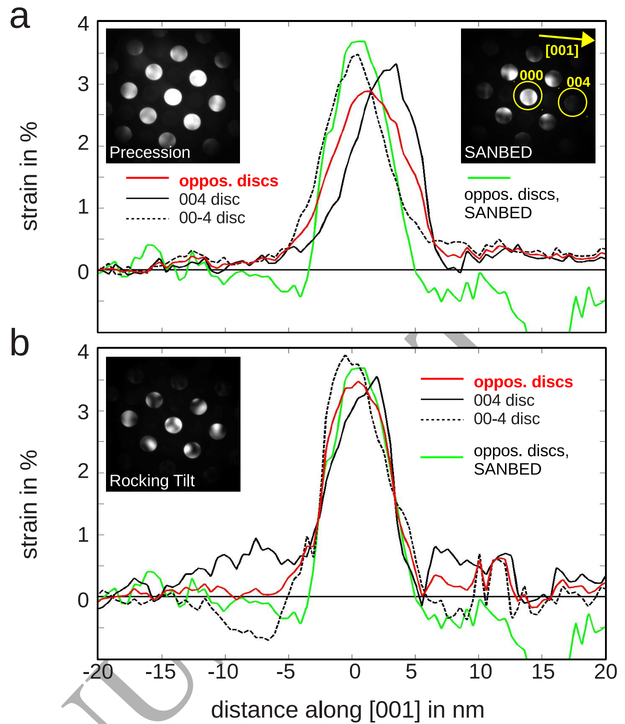

Figure 8: Experimental strain profiles from NBED series using (a) precession-like summation of 12 tilts and (b) rocking-beam with two tilts in [001] and [00$\bar{1}$] direction. NBED patterns are exemplarily shown in (a) and (b). Red curves show evaluations from opposite discs, black curves single-disc evaluations. The green curves show the strain from a standard SANBED evaluation without tilt.

direction ($b = 0$; $|c| = 2$) are always part of the series. In analogy to (non-discrete) electron precession, this summation over discrete tilts is denoted as *precession-like* in the following. To keep the evaluations comparable, in all summed patterns the same number of electrons N_e for the simulation of noise was used. Obviously, the measured strain profiles in Fig. 7 are very similar for all n. The green profiles in Fig. 7 show the real strain for comparison.

The green circles in the right part of Fig. 6 show the precision for the five profiles in Fig 7. As visible from the NBED patterns in Fig. 7, the intensity distributions within all NBED discs become more and more homogeneous with increasing n. The green circles in the right part of Fig. 6 show the precision for the five profiles in Fig. 7 in case of a single-disc evaluation with the 004 disc. Obviously, the precision of the strain measurement is not significantly improved with increasing number n of summed images. An explanation could be that summing more images not only leads to a more homogeneous intensity distribution in the 004 disc - but also to a distribution of intensity into all other discs. Consequently, the Poisson noise in the evaluation of the 004 disc increases which reduces the precision. As those other discs are not evaluated, the summation of many images does not lead to a better precision. Calculating the strain from opposite discs gives a better precision as shown by the five square markers directly below the green circles in Fig 6. This result shows that for the described simulation with an azimuthal tilt of 7 mrad in combination with the used single-disc detection algorithm, precession-like summation is not significantly affected by the number n of tilt angles (for $2 \leq n \leq 32$) in terms of a reduction of appearing strain features or a strong improvement of the precision.

In case of structures where the composition changes only along one spatial direction, as this is the case for the InGaAs layer in GaAs presented here, only the strain along this direction is of interest (here, the strain in [001] growth direction). The idea of precession-like summation would then be optimized for a rocking beam with two tilts only in [001] and [00$\bar{1}$] direction instead of a full precession circle. The experimental implementation of the rocking beam as well as the precession-like summation was done using scripting as demonstrated in the appendix of Ref. [46]. Three different experimental setups were compared. First, a precession-like summation of 12 tilts lying on a circle with 30° between them with an absolute tilt of approximately 7 mrad. A corresponding NBED pattern is shown in the left inset of Fig. 8a. Second, a rocking beam between two tilts, with 7 mrad in [001] and [00$\bar{1}$] direction (corresponding NBED pattern in Fig. 8b). Third, a standard NBED setting without any tilt (corresponding NBED pattern in the right inset of Fig. 8a).
The black profiles in Figs. 8a and b show the strain for single-disc evaluation of the 004 and the 00$\bar{4}$ disc. The

red profile shows the opposite-discs evaluation, for (a) the precession-like summation and (b) the rocking beam case. The green curves in both figures (a,b) show the evaluation of the standard NBED series without tilt from opposite-discs evaluation. In Fig. 8a, the position of the strained layer in the 004 profile is shifted relatively to the one in the 00$\overline{4}$ profile. This shift is caused by a misalignment as the beam tilt (controlled by the *rotation center* for the Titan microscope) led to a small shift of the probe on the specimen which could not entirely be corrected. For the summation of two tilts in Fig. 8b, the effect is obviously smaller. Similar as for the simulation in Fig 5b, the black 004 profile in Fig. 8b shows a *hill* on the left-hand side of the InGaAs layer where the black 00$\overline{4}$ profile shows a *dip*. The strain profile from opposite-discs evaluation (red) is more flat with less strain features compared to the standard evaluation (green). It is important to mention that in this experimental realization of the rocking-beam concept only a single scan was evaluated for each type of method. As shown in Sec. 3.1, there might be deviations between line scans carried out at slightly different specimen positions. The fact that the profiles in Fig. 8 do not perfectly show the expected symmetries can be attributed to this. Concluding, the suggested rocking-beam approach has the potential to significantly optimize strain measurements from NBED disc-detection. The presented experimental implementation via scripting is mainly limited by the restricted access to the microscope's alignment procedures over an external software. However, the positive results suggest further development in this field.

5. Towards high-convergence SANBED

The strain analysis by the SANBED method is limited by the maximum convergence angle as free space in between the NBED discs is necessary to guarantee a detection of the discs by the suggested routines. In consequence, for materials with relatively large lattice constants, the convergence of the probe has to be reduced down to very low angles which might undesirably increase the probe size and possibly decrease the discs' shape. Therefore, it would be beneficial to perform NBED strain analysis also at higher convergence angles.

In Sec. 5.1 the realization of strain analysis for higher-convergence NBED for experiment and simulation is presented by the use of a special probe-forming aperture with a cross in its center. Sec. 5.2 deals with the question whether a higher convergence angle - and consequently a smaller probe size - in general improves spatial resolution in case of standard evaluation techniques.

5.1. Structured probe-forming aperture

Depending on the combination of material system and applied probe convergence, discs in the NBED pattern may overlap. The standard methods for disc detection might

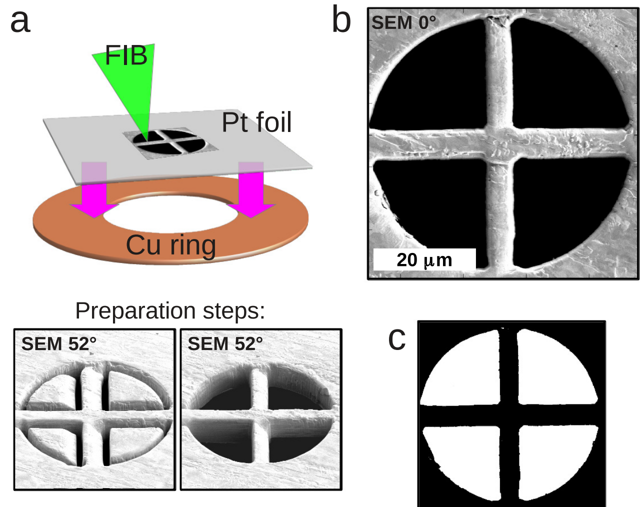

Figure 9: (a) Schematic of a cross-aperture design: a 7.5 μm thick Pt foil was fixed on a copper ring and a cross pattern was etched into the foil using a focused-ion beam. SEM images show two preparation steps. (b) SEM image of the final cross structure. (c) Black-white image from conversion of the SEM image in (b) which was used as aperture function in the simulation.

fail as the border of the discs become less defined and the intensity difference between *inside* and *outside* of the disc can become completely non-trivial. Furthermore, the intensity distribution within the overlap region strongly depends on local specimen parameters such as thickness and chemical concentration. In order to investigate also series of higher convergence, an approach was applied utilizing an idea that was theoretically suggested in Ref. [53]: the usage of a structured probe-forming aperture. Instead of a round aperture, an aperture with a cross inside was used, which creates characteristic crosses in the centers of all NBED discs. By detecting these crosses, the disc-edge regions do not have to be considered for detection of the positions of the discs.

For the experimental implementation, a 7.5 μm thick platinum foil (Goodfellow, type PT000210) was attached on top of a copper ring as shown in the schematic in Fig. 9a. The copper ring was made by gluing two TEM grids (each with a central 1.5 mm hole) on top of each other for better mechanical stability. In order to guarantee electrical conduction, gold was deposited on the final structure using vacuum deposition. The structure shown in the scanning-electron microscopy (SEM) image in Fig. 9a and b was cut into the foil by focused ion-beam etching. The visible outer ring has a diameter of 50 μm to be comparable to the standard hole aperture in our microscope. The cross' ridges have a width of approximately 12 % of this diameter. After plasma-cleaning of the fabricated aperture, it was mounted into the C2-aperture holder.

Fig. 10a shows experimental NBED patterns for three different semi-convergence angles of 2.6, 3.3 and 4.7 mrad where the first two patterns show separated discs but the

ACCEPTED MANUSCRIPT

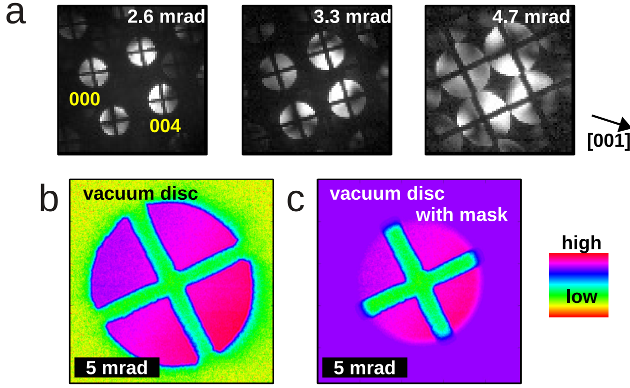

Figure 10: (a) Experimental NBED patterns using the cross aperture for semi-convergence angles of 2.6, 3.3 and 4.7 mrad. (b) The central NBED disc in vacuum was recorded and a patch slightly larger than the visible diameter was cut (vacuum disc). (c) The outer part of the vacuum disc shown in (b) was covered by a smooth mask as only the central cross should be tracked. The outside level was set to the mean intensity at the mask's radius.

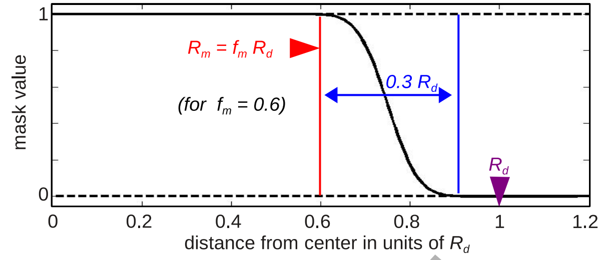

Figure 11: Visualization of the applied mask with a smooth edge. Shown is a 1-dimensional profile from the center of the mask to a distance 1.2 times the estimated disc radius R_d. The transition region where the error function drops from 1 to 0 has a width of 30 % of the discs radius. The mask radius which is the onset of the transition region is $R_m = f_m \cdot R_d$ with a factor $f_m = 0.6$ in this example.

third one shows discs which start to overlap - those discs could not be evaluated by the standard disc detection procedure. The sample was tilted to slightly excite the 004 disc. For all cases, the characteristic cross is visible in all discs. The relative rotation between the cross' arms and growth direction is approximately 45° but it slightly changes with convergence setting as visible from Fig. 10a.

For each convergence angle, six line profiles of 160 steps over 40 nm were recorded. The strain evaluation was performed as follows: After acquisition of the series along a line scan, the central disc was recorded without specimen (*vacuum disc*). A squared patch slightly larger than the disc diameter was cut around the 000 and the 004 discs in all images and around the vacuum disc. The relative positions of the discs were finally determined from cross correlating each disc patch with the patch of the vacuum disc. To be sure that the cross correlation is dominated by the inner cross and not by the disc edge, a mask based on a circular window function with a smooth edge was applied to all patches. The mask was rotationally symmetric with the shape of an error function: starting in the center, the mask value is 1 up to the mask radius $R_m = f_m \cdot R_d$ with the estimated disc radius R_d and a factor $0 \leq f_m \leq 1$. At the distance R_m, a the transition region follows with a width of 30 % of the discs radius in which the mask value drops from 1 to approximately 0. Due to the symmetry of the error function the mask value is 0.5 at the distance $R_m + 15\,\% \cdot R_d$. To avoid the cross correlation to be affected by the mask radii itself, the factor f_m for the disc patch was chosen differently than for the vacuum disc. It turned out that best strain profiles were obtained for an f_m for the diffraction-disc patches between 20 % and 55 % in combination with an f_m for the vacuum disc being 1.4-1.6 times larger. The vacuum disc is exemplarily shown in Fig. 10b without masking and in Fig. 10c with an applied mask with a factor $f_m = 50\,\%$.

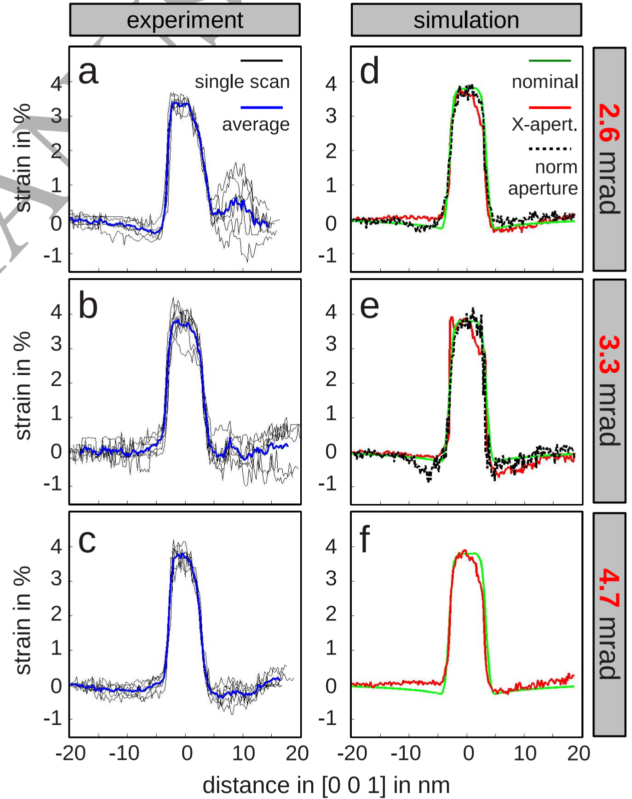

Figure 12: Strain measured from NBED series for experiment (left column, a-c) and for simulations (right column, d-f) for semi-convergence angles of 2.6 mrad (a,d), 3.3 mrad (b,e) and 4.7 mrad (c,f). For experimental data, the strain from single line scans is shown (black) as well as from the average over all single scans (blue). In case of the simulations, the green profiles show the real strain in the super cell and the red profiles the strain measured from simulated NBED patterns with a cross aperture. The black dashed curves show standard SANBED results from simulations with a hole aperture - this method expectedly did not work for a convergence angle of 4.7 mrad.

ACCEPTED MANUSCRIPT

For the three convergence angles Figs. 12a-c show the experimental strain from all single scans as well as for the average of all scans. A mask factor of f_m=40 % for the disc patches and of f_m=65 % for the vacuum disc were used. Obviously, the characteristic strain features on both sides of the InGaAs layer are not identical for the convergence angles. As shown in Sec. 3.1, this effect is very sensitive to the exact crystal orientation. As the beam settings had to be changed for changing the convergence angle, the profiles for different convergences can probably not be compared in terms of exact zone axis or excitation of the discs. But Figs. 12a-c show that with the used cross-aperture approach a strain analysis is possible even for high convergence angles with contacting discs (Fig. 12c).

For a comparison with simulations, the NBED series was simulated using multislice simulations. To mimic a realistic probe, the SEM image shown in Fig. 9b was reduced to a black-white image shown in Fig. 9c. With black interpreted as 0 and white as 1, the image was used as aperture function in the simulation. For a better comparison to experiment, the aperture was rotated to achieve a relative rotation between growth direction and the cross' arms of 45°. The strain determination was identical to the evaluation of the experimental series by applying a mask with factor of f_m=40 % for the disc patches and of f_m=60 % for the (simulated) vacuum disc. The resulting strain is shown by the red profiles in Figs. 12d-f. Obviously, the profiles are in good agreement with the real strain shown by the green curves. The identical simulations were performed with a standard hole aperture instead of the cross aperture. The disc detection for the highest convergence angle expectedly failed. The strain profiles for 2.6 and 3.3 mrad semi-convergence angle are shown in Fig. 12d-e by the black dashed line. Deviations of the obtained profiles to the real strain are of the same magnitude compared to those for the red profiles which confirm the applicability of the cross aperture.

5.2. Spatial resolution: a theoretical consideration

In this section the principle effect of beam convergence on the spatial resolution of the NBED technique is investigated by means of simulations. As shown in Sec. 5.1, the disc-detection routines used for SANBED are not able to detect overlapping discs, so the crystal lattice limits the size of the applied probe convergence angle. Furthermore, propagation through the specimen and channelling in the crystal might also affect spatial resolution. To overcome these effects and to restrict the focus on the influence of the probe convergence, an idealized simulation was designed which neglects all crystal effects and only contains interfaces between two regions each having different abilities to shift the central disc. The ability to shift the central disc can be seen in analogy to the amount of strain in a crystal which leads to a shift e.g. of the 004 disc. This was accomplished by a simulation similar to those presented in Sec. 3 with an *empty* supercell reduced to a single slice (region A) which does not contain any atoms but

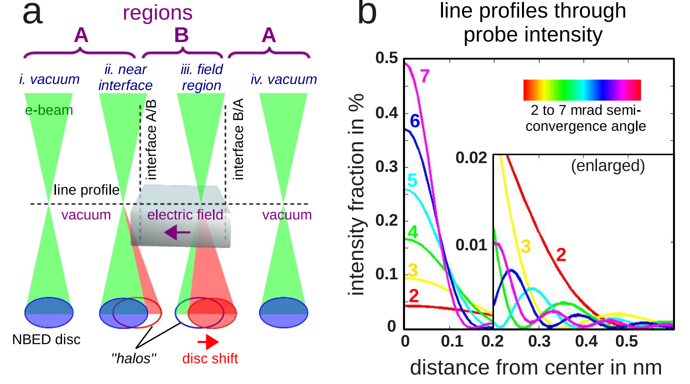

Figure 13: (a) Schematic of the simulation: NBED patterns are recorded for a series where the probe is scanning over a thin region B inside the surrounding region A. Both, region A and B do not contain any specimen (vacuum) but region B contains an electric field. Shown are four scan positions of the electron probe: Within region A the central disc is in the center of the diffraction pattern (*i,iv*) and within region B the disc is shifted (*iii*). Close to the interface in region A the electron probe is leaking into the field region causing the *halo* effect *ii*. (b) Line profiles through the intensity of simulated electron probes as a function of the distance to the probe's center. Different line colors show semi-convergence angles between 2-7 mrad. For better visibility, the intensity axis is enlarged from 0.2 nm away from the center.

an inserted region B in which a constant electric field was added as shown in the schematic in Fig. 13a. The strength of this field was chosen to shift the disc by a maximum of 200 µrad assuming a direct connection of transferred momentum Δp and the field strength E times the thickness of the super cell t [54]:

$$\Delta p = \frac{-e}{v} E t \; , \tag{2}$$

where v is the velocity of the beam electrons.

NBED simulations were performed for semi-convergence angles of the used probe between 2 and 7 mrad in steps of 1 mrad. The applied defocus for each convergence angle was chosen to maximize the intensity in the center of the probe. This defocus Δf as function of the semi-convergence angle θ_{sc} is shown in Fig. 15 and can be parametrized by the equation

$$\Delta f(\theta_{sc}) = c_p \theta_{sc}^2 \tag{3}$$

with the coefficient c_p = -0.6 $\frac{\text{nm}}{\text{mrad}^2}$ for the used acceleration voltage of 300 kV and a spherical-aberration constant of 1.2 mm.

Line profiles through the intensity of simulated electron probes as a function of the distance to the probe's center. Different line colors show semi-convergence angles between 2-7 mrad. For better visibility, the intensity axis is enlarged from 0.2 nm away from the center.

Fig. 13b shows line profiles through the intensity of simulated electron probes. The higher the convergence, the closer the intensity is concentrated at the center of

ACCEPTED MANUSCRIPT

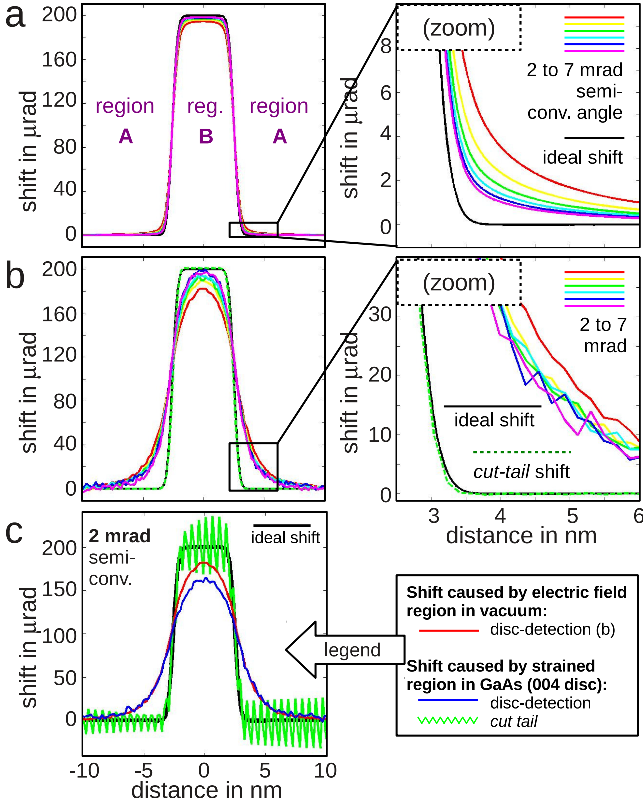

Figure 14: Profile of the shift of the NBED disc due to the influence of the electric field inside region B (see schematic in Fig. 13a) for different semi-convergence angles (line color). The black profiles in a-c show the ideal shift which is directly proportional to the field strength. (a) Expected optimum disc shift from convolution of the black profile with the intensity profiles of the electron probes. (b) Disc shift for a scan over the regions A-B-A determined by the disc-detection routine. Dashed-green profile shows the case for an electron probe with a semi-convergence angle of 2.6 mrad for which the tail of the electron probe was cut off (meaning of *tail* here: all intensity outside the first minimum of the probe). This completely removes the *halo* effect. (c) Comparison to a strain measurement (for 2 mrad semi-convergence angle only). The red profiles show the cases shown in a and b: for convolution with the probe intensity (dashed) and from disc detection (solid line). The blue curve shows the measured shift of the 004 disc in case of a GaAs super cell with a thickness of 10 nm containing strain of maximum 1.44 % instead of an electric field in the region B.

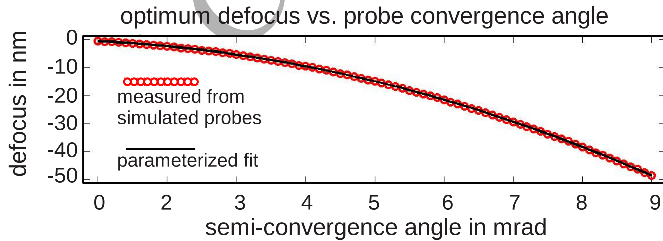

Figure 15: Applied defocus which maximizes the intensity in the center of the probe as function of the probe's semi-convergence angle. Red data points: measurement from simulated probes. Solid line: fit of the data points parametrized by equation 3.

the probe. One can assume that the disc-detection routine itself has an influence on the spatial resolution with which the sharpness of an interface can be measured. The sharpest interface for a measurement with a given electron probe is given by the convolution of the interface with the shape of the probe intensity. The black profiles in Figs. 14a-c show the ideal shift of the CBED disc given by Eq. 2. The coloured curves in Fig. 14a were derived from the convolution of this ideal curve with electron probes with semi-convergence angles between 2 and 7 mrad. For all probes the profiles are broadened but the deviation from the ideal (black) curve is decreasing with convergence angle. The broadening effect can be described by the term ζ which is the sum of the absolute deviation between the broadened profile and the ideal (black) profile divided by the sum of the ideal profile. This value was calculated over the spatial region from -5 nm to 5 nm. For the semi-convergence angles 2-7 mrad in Fig. 14a, ζ has the values in % of: 6.9, 4.6, 3.5, 2.8, 2.4, and 2.1.

Fig. 14b shows (with the same meaning of the line style as in Fig. 14a) the shift of the central disc for a scan over the regions A-B-A measured using disc detection. Obviously, these profiles are broadened much stronger compared to those from probe-convolution in Fig. 14a. Deviations between different convergence angles are negligible compared to the absolute deviation to the black curve. The corresponding ζ values in % for the semi-convergence angles 2-7 mrad are: 35.4, 30.1, 27.7, 26.2, 23.5, and 22.8.

The strong deviation between the measured disc position and the black curve in Fig. 14b can be explained by the fact that the electron probe interacts with region B even for scanning positions within region A far away from the interface - and vice versa. In consequence, the shape of the NBED disc is influenced as it was described in Ref. [29] and denoted there as *halo*-effect: The electron probe is not an ideal spot but has a spatial extension with the shape of an Airy function as the intensity distribution mathematically results from the Fourier transform of the probe-forming hole-shaped aperture. The outer parts of the function (the *tail*) for a scan position in region A leaks into region B, thus the resulting NBED pattern contains a contribution of a shifted disc stemming from this region. As the probe's tail corresponds to high spatial frequencies of the probe forming aperture, the outer part of the electron probe contains information formed by the sharp edge of the aperture. Consequently, the shifted contribution to the final overlay NBED pattern is not disc-shaped but ring-shaped and, according to this aspect the effect is called a *halo*. An NBED disc without visible halo from region A is shown in Fig. 16a. Fig. 16b shows a disc from region B with a characteristic halo visible on the left-hand side of the disc.

In order to check whether the broadening actually stems from the halo effect, a modified simulation was performed. The probe's tail was cut away at the first intensity minimum to avoid leaking of intensity from region A into region B. As a consequence, an NBED disc with defined edges is

ACCEPTED MANUSCRIPT

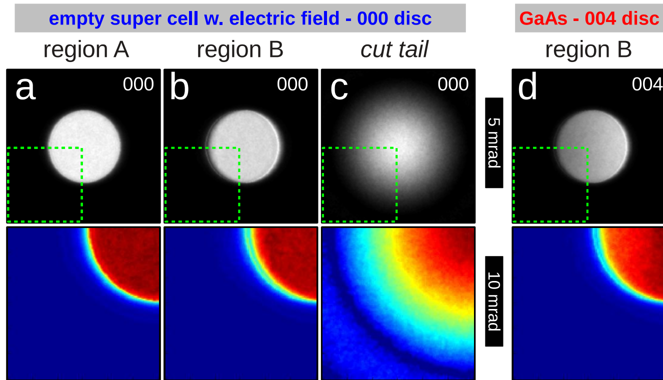

Figure 16: NBED discs from simulations: (a-c) the central disc from an empty super cell with an electric field as shown in the schematic in Fig. 13a and (d) the 004 disc from a GaAs super cell. The semi-convergence angle was 2 mrad in (a,b,d) and 2.6 mrad in (c). Scan positions: (a) within region A (no field), (b) in region B (electric field), (c) region A, (d) region B (with strain). Lower images show magnified quarter marked by the dashed boxes in the upper images with square-root of intensity.

not observed. Instead, the intensity is radially decreasing as shown in Fig. 16c. The disc-detection was therefore performed by cross correlation using the NBED disc of the first scan position instead of a ring-shaped mask. The dashed-green profile in Fig. 14b shows the shift measured from this simulation for 2.6 mrad semi-convergence angle. The profile is hardly to distinguish from the ideal (black) curve showing that the observed broadening stems from the spatial expansion of the electron probe and the halo-effect. As visible from the coloured curves in Fig. 14b, the broadening caused by the halo effect is similar for all convergence angles. The broadening can roughly be described by a convolution of the ideal (black) profile with a Gaussian function with σ=1.2 nm.

Due to the negligence of crystal and propagation effects the presented simulations might overrate the influence of the halo effect on the interface broadening. In order to investigate how realistic the simulations are in terms of interface broadening, a standard simulation with a GaAs super cell was performed for a semi-convergence angle of 2 mrad. The super cell had a thickness of 10 nm in electron-beam direction and contained a strain distribution along the scan direction with exactly the same shape as the field distribution in the previous simulation. The maximum strain in region *B* was chosen to cause an expected shift of 200 μrad of the 004 disc (approximately 1.44 % strain). Fig. 16d shows the 004 disc from the NBED pattern from region *B*: the disc is shifted with a halo visible on the left-hand side. The measured shift of the 004 disc from scanning over the regions *A*-*B*-*A* is shown by the blue curve in Fig. 14c. The red curve in Fig. 14c shows the results from disc detection for the idealized simulations with an electric field for 2 mrad (identical to the red curve in Fig. 14b). Obviously, both profiles obtained from disc detection, the blue and the solid-red one, show a comparable broadening which indicates that the used model system with an electric field realistically describes the interface broadening by the halo effect. The green curve in Fig. 14c shows the result of the 004 disc detection in GaAs in case of a cut-off probe tail. The broadening completely vanishes but oscillations occur as the probe now resolves single atomic columns.

For both curves, the red one (electric field) and the blue one (strain in GaAs), the broadening caused by the halo effect is so strong that the maximum disc shift of 200 μrad in the center of the well is not reached. In case of a strain analysis a wrong maximum strain would be measured. In the following, the influence of the halo on NBED strain analyses from different diffraction discs is evaluated. Fig. 17 shows the measured strain determined from disc-detection based on the simulation of the strained layer in GaAs for a semi-convergence angle of 2 mrad. The black curve shows the input strain, the coloured curves the strain from evaluating the 004 disc (blue), the 008 disc (red) and the 00(12) disc (green). The dashed curve shows the strain from a simulation with reasonable noise in the NBED patterns, the solid curves show the strain from a simulation without noise. The broadening of the profile for the 004 disc (ζ=36 %) is stronger than for the 008 disc (ζ=22 %). The broadening outside the central layer is further decreased for the 00(12) disc as it can be seen from the zoomed inset in Fig. 17. The ζ value of 22 % for the green curve is not increased compared to the red curve as the deviation from the black curve is stronger within the layer - which shows that the disc detection becomes difficult for weakly excited discs as it is the case for the 00(12) disc. That the broadening for the evaluation of the 008 disc is reduced compared to the lower order 004 disc can be explained by the fact that the distance between the diffracted disc belonging to the material under the center of the electron probe and the halo increases for higher order discs. Due to the spatial separation of halo and disc in the NBED patterns, the used detection routines can find the disc position more accurately. Otherwise, the detection is hindered as the electron intensity drastically decreases for higher order discs. The strain precision for the profile evaluating the 008 disc is 1.5 times worse than for evaluating the 004 disc. The precision for evaluating the 00(12) disc is even more than 4 times worse than for evaluating the 004 disc. Nevertheless, the spatial resolution of the NBED strain analysis based on the used detection algorithms can be improved by evaluating higher order discs.

In conclusion, in case of NBED-disc detection using standard evaluation routines, the halo effect strongly reduces the spatial resolution when scanning over an interface which is in agreement with former studies [29]. Compared to this effect, the influence of the probe's convergence angle on spatial resolution is much weaker and even negligible for semi-convergence angles larger than approximately 3 mrad. The broadening of strain profiles caused by the halo effect is decreasing for the evaluation

ACCEPTED MANUSCRIPT

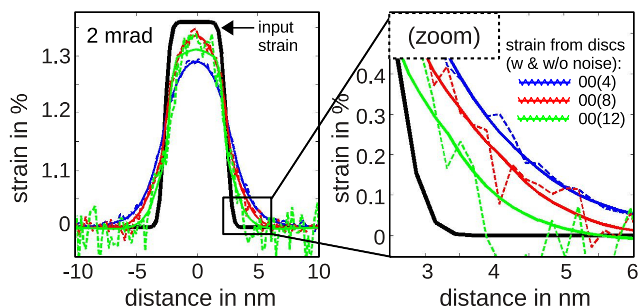

Figure 17: Strain from NBED-disc detection for a scan over a 10 nm thick GaAs super cell with a strained layer inside (strain distribution shown by the black curve). Coloured curves show the results from evaluating the 004 disc (blue), the 008 disc (red) and the 00(12) disc (green). Simulations were performed with noise (dashed curves) and without noise (solid curves).

of higher order NBED discs.

6. Summary

The first part of this study in Sec. 3 dealt with the simulation of NBED series for strain analysis using the SANBED [16] method. In Sec. 3.1 experimental strain profiles for an InGaAs layer in GaAs recorded for different specimen tilts were compared to strain profiles obtained from a simulated crystal. The comparison indicated that the used simulations in general are able to describe an experimental strain measurement. It was shown that the maximum strain in the InGaAs layer represents the strain in the crystal averaged over the complete thickness of 55 nm in case of a strong excitation of the evaluated 004 disc. An excitation of the 004 disc improved the precision and reduced the occurrence of strain features. Even better results were obtained when the specimen is additionally tilted perpendicular to the [001] growth direction. Based on this validated simulations, in Sec. 4 the dependence of characteristic strain features on the applied specimen tilt was investigated more closely. Sec. 4.1 shows that the measured averaged strain in the InGaAs layer as well as the occurrence of strain *dips* next to the layer strongly depend on the applied tilt in [001] growth direction. In Sec. 4.2 it turned out that the evaluation of the 004 disc and the $00\bar{4}$ disc result in two different strain profiles. A similar effect occurred for the same evaluation from two separate NBED patterns each with a tilt that strongly excites the evaluated 004 disc or the $00\bar{4}$ disc, respectively. The best agreement with the underlying strain was obtained for evaluating the distance between the opposite discs, 004 and $00\bar{4}$, which also improved precision. Based on simulations it was shown that in case of a precession-like setup where the NBED pattern stems from a summation of up to 32 discrete tilts lying on a circle (with the tilt towards [001] direction being always part of the summation), the number of tilts does neither significantly influence the strain profile nor the precision for the evaluation of the 004 disc. Consequently, a *rocking-tilt* method was suggested which reduces the number of tilts to two: towards the [001] and $[00\bar{1}]$ directions. It was realized in an experiment by scripting, allowing to tilt the beam, to back-shift the diffraction pattern and correct for beam movement, resulting in an NBED pattern combining the two tilts. It could be shown that this *rocking-tilt* method indeed gives less strain artifacts compared to the standard, non-tilted experiment.

In Sec. 5 the increase of the probe-convergence angle on the strain measurement was investigated. In Sec. 5.1, a probe-forming aperture with an additional cross inside was experimentally realized. As the aperture's cross was visible in all discs within the NBED patterns, the cross was detected instead of the complete disc and strain could be evaluated for different convergence angles - even for the case when discs started to overlap.

In Sec. 5.2 it is discussed whether higher convergence angles can theoretically increase the spatial resolution. NBED simulations for different convergence angles for an idealized specimen were performed: The super cell did not contain any atoms but an inserted region with a homogeneous electric field which shifted the central NBED disc. It turned out that for the used disc-detection routines the spatial resolution is strongly reduced for all convergence angles in a way that the influence of beam convergence becomes almost negligible. It was proven that the strong reduction of the spatial resolution can be explained by the *halo* effect [29] caused by the fact that intensity far away from the center of the electron probe leaks into distinct specimen regions thus leading to an overlay of information from different spatial positions within the NBED pattern. It could be shown that the halo effect is weaker for the 008 and the 00(12) disc due to the separation between disc and halo in the NBED pattern. Consequently, in case of the used detection routines, spatial resolution can be improved by evaluating higher order NBED discs.

Acknowledgements

This work was supported by the German Research Foundation (DFG) under Contracts RO2057/11-1 and RO2057/12-1.

Appendix A. Measurement of the indium concentration and the specimen thickness for the investigated specimen

In order to determine the indium concentration in the investigated specimen, a chemical analysis of the InGaAs layer was performed using quantitative HAADF STEM. This technique is based on a direct comparison of the HAADF-STEM intensity averaged over a crystal unit cell with multislice simulations. A detailed explanation of the

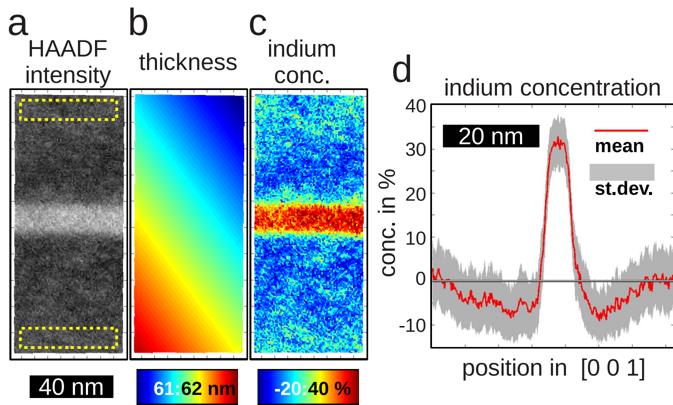

Figure A.18: Quantitative HAADF-STEM concentration analysis of the investigated specimen. Shown are the derived maps for (a) HAADF intensity, (b) specimen thickness and (c) indium concentration as well as (d) the average indium concentration as profile (standard deviation shown in gray). The dashed boxes in (a) mark the regions of pure GaAs used for interpolating the background intensity (see text). The scale bar below (a) is valid for (a-c).

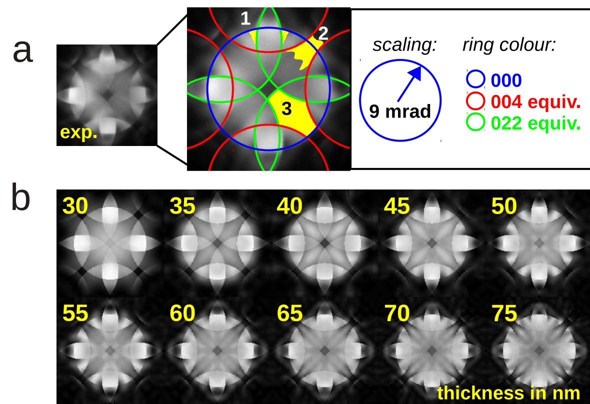

Figure A.19: PACBED evaluation to estimate the specimen thickness. (a) Experimental PACBED image with a schematic in which three regions are pointed out where the intensity characteristically changes with thickness (yellow, numerated with 1-3). (b) Simulation of PACBED images for GaAs for thicknesses between 30 nm to 75 nm.

simulations and the evaluation can be found in Ref. [55, 56]. Fig. A.18a shows an HAADF-STEM image in which the dashed boxes mark regions of pure GaAs. Based on the intensity in these two regions, the *background intensity* is interpolated to the complete image and the local thickness is derived from a direct comparison with simulated intensities for pure GaAs. As it can be seen from Fig. A.18b, the thickness within the evaluated image is almost constant (color scaling between 61-62 nm). With known thickness at every image point, the indium concentration is derived from the comparison of the HAADF intensity to simulations for different concentrations. The indium-concentration map and its averaged profile are shown in Fig. A.18c and Fig. A.18d, respectively. The indium concentration on both sides of the central InGaAs layer is artificially decreased due to a reduction of the HAADF-STEM intensity. The reason for this effect is a long-ranging surface-strain field caused by the relaxation of the lamella along the [100] electron-beam direction. This is connected with the bending of the (001) lattice planes which leads to a reduced electron channelling and consequently to less HAADF intensity [44]. The concentration values in the surface-strained regions do of course not represent the real indium concentrations. But, due to the symmetry of the layer structure, the central part in the InGaAs should not be affected by the surface strain fields (see e.g. [56]). The central indium concentration is approximately 31 %. The linearly interpolated lattice constant of InGaAs with 31 % indium is 2.2 % larger compared to GaAs for bulk material - but in case of tetragonal distortion, the lattice constant in growth direction in the InGaAs layer can be up to 4.3 % larger (biaxial case) compared to the GaAs substrate.

The quantitative HAADF-STEM analysis was performed at a position on the TEM lamella slightly different to those where the strain-measurements were performed. The thickness in the region where the experimental NBED series were recorded was determined using PACBED. Fig. A.19(a) shows an experimental GaAs PACBED image of this region. PACBED simulations for GaAs in [100] electron-beam direction were performed using the absorptive-potential multislice approach [35, 36] in the STEMsim program [37]. A comparison to simulations which are shown in Fig. A.19(b) gives a thickness of 54±2 nm. As the changes in the PACBED pattern are small, the specific regions in the pattern where characteristic changes occur are schematically shown in the enlarged pattern in Fig. A.19(a).

References

[1] A. Lenz, H. Eisele, R. Timm, L. Ivanova, R. L. Sellin, H.-Y. Liu, M. Hopkinson, U. W. Pohl, D. Bimberg, M. DÃďhne, Limits of In(Ga)As/GaAs quantum dot growth, Physica Status Solidi B 246 (2009) 717–720.

[2] S. B. Desai, G. Seol, J. S. Kang, H. Fang, C. Battaglia, R. Kapadia, J. W. Ager, J. Guo, A. Javey, Strain-Induced Indirect to Direct Bandgap Transition in Multilayer WSe2, Nano Letters 14 (2014) 4592–4597.

[3] J. Welser, J. Hoyt, G. J.F., Electron mobility enhancement in strained-Si n-type metal-oxide-semiconductor field-effect transistors, Electron Device Lett 15 (1994) 100–102.

[4] I. Ferain, C. Colinge, J.-P. Colinge, Multigate transistors as the future of classical metal-oxide-semiconductor field-effect transistors, Nature 479 (2011) 310–316.

[5] M. J. Hÿtch, E. Snoeck, R. Kilaas, Quantitative measurement of displacement and strain fields from HREM micrographs, Ultramicroscopy 74(3) (1998) 131–46.

[6] A. Rosenauer, T. Remmele, D. Gerthsen, K. Tillmann, A. Förster, Atomic scale strain measurements by the digital analysis of transmission electron microscopic lattice images, Optik 105 (1997) 99.

[7] P. L. Galindo, S. Kret, A. M. Sanchez, J.-Y. Laval, A. Yanez, J. Pizarro, E. Guerrero, T. Ben, S. I. Molina, The Peak Pairs algorithm for strain mapping from HRTEM images, Ultramicroscopy 107 (2007) 1186 – 1193.

[8] A. M. Sanchez, P. L. Galindo, S. Kret, M. Falke, R. Beanland, P. J. Goodhew, Quantitative Strain Mapping Applied to Aberration-Corrected HAADF Images, Microscopy and Microanalysis 12 (2006) 285–294.

ACCEPTED MANUSCRIPT

ACCEPTED MANUSCRIPT

[9] T. Grieb, K. Müller, R. Fritz, M. Schowalter, N. Neugebohrn, N. Knaub, K. Volz, A. Rosenauer, Determination of the chemical composition of GaNAs using STEM HAADF imaging and STEM strain state analysis, Ultramicroscopy 117 (2012) 15 – 23.

[10] M. Hÿtch, F. Houdelier, F. Hue, E. Snoeck, Nanoscale holographic interferometry for strain measurements in electronic devices, Nature 453 (2008) 1086.

[11] C. T. Koch, V. B. Özdöl, P. A. van Aken, An efficient, simple, and precise way to map strain with nanometer resolution in semiconductor devices, Applied Physics Letters 96 (2010) 091901.

[12] K. Usuda, T. Mizuno, T. Tezuka, N. Sugiyama, Y. Moriyama, S. Nakaharai, S. ichi Takagi, Strain relaxation of strained-Si layers on SiGe-on-insulator (SGOI) structures after mesa isolation, Applied Surface Science 224 (2004) 113–116.

[13] K. Usuda, T. Numata, T. Irisawa, N. Hirashita, S. Takagi, Strain characterization in {SOI} and strained-Si on {SGOI} {MOSFET} channel using nano-beam electron diffraction (NBD), Materials Science and Engineering: B 124 (2005) 143–147.

[14] A. Béché, J.-L. Rouvière, L. Clement, J. Hartmann, Improved precision in strain measurement using nanobeam electron diffraction, Applied Physics Letters 95 (2009) 123114.

[15] F. Uesugi, A. Hokazono, S. Takeno, Evaluation of two-dimensional strain distribution by STEM/NBD, Ultramicroscopy 111 (2011) 995 – 998.

[16] K. Müller, A. Rosenauer, M. Schowalter, J. Zweck, R. Fritz, K. Volz, Strain Measurement in Semiconductor Heterostructures by Scanning Transmission Electron Microscopy, Microscopy and Microanalysis 18 (2012) 995–1009.

[17] S.-W. Kim, D.-S. Byeon, H. Jang, S.-M. Koo, H.-J. Lee, D.-H. Ko, Strain characterization of fin-shaped field effect transistors with SiGe stressors using nanobeam electron diffraction, Appl. Phys. Lett. 105 (2014) 083104.

[18] F. Uesugi, Strain mapping in selected area electron diffraction method combining a Cs-corrected TEM with a stage scanning system, Ultramicroscopy 135 (2013) 80–83.

[19] J. Liu, K. Li, S. Pandey, F. Benistant, A. See, M. Zhou, L. Hsia, R. Schampers, D. Klenov, Strain relaxation in transistor channels with embedded epitaxial silicon germanium source/drain, Appl. Phys. Lett. 93 (2008) 221912.

[20] D. Cooper, T. Denneulin, J.-P. Barnes, J.-M. Hartmann, L. Hutin, C. L. Royer, A. Béché, J.-L. Rouvière, Strain mapping with nm-scale resolution for the silicon-on-insulator generation of semiconductor devices by advanced electron microscopy, Journal of Applied Physics 112 (2012) 124505.

[21] K. Müller, H. Ryll, I. Ordavo, M. Schowalter, J. Zweck, H. Soltau, S. Ihle, L. Strüder, K. Volz, P. Potapov, A. Rosenauer, STEM strain analysis at sub-nanometre scale using millisecond frames from a direct electron read-out CCD camera, Journal of Physics: Conference Series 471 (2013) 012024.

[22] A. Béché, J. Rouvière, J. Barnes, D. Cooper, Strain measurement at the nanoscale: Comparison between convergent beam electron diffraction, nano-beam electron diffraction, high resolution imaging and dark field electron holography, Ultramicroscopy 131 (2013) 10 – 23.

[23] F. Baumann, High precision two-dimensional strain mapping in semiconductor devices using nanobeam electron diffraction in the transmission electron microscope, Appl. Phys. Lett. 104 (2014) 262102.

[24] K. Müller-Caspary, A. Oelsner, P. Potapov, Two-dimensional strain mapping in semiconductors by nano-beam electron diffraction employing a delay-line detector, Applied Physics Letters 107 (2015) 072110.

[25] V. Ozdol, C. Gammer, X. Jin, P. Ercius, C. O. J. Ciston, A. Minor, Strain mapping at nanometer resolution using advanced nano-beam electron diffraction, Appl. Phys. Lett. 106 (2015) 253107.

[26] T. C. Pekin, C. Gammer, J. Ciston, A. M. Minor, C. Ophus, Optimizing disk registration algorithms for nanobeam electron diffraction strain mapping, Ultramicroscopy 176 (2017) 170–176.

[27] J.-L. Rouvière, A. Béché, Y. Martin, T. Denneulin, D. Cooper, Improved strain precision with high spatial resolution using nanobeam precession electron diffraction, Applied Physics Letters 103 (2013) 241913.

[28] M. P. Vigouroux, V. Delaye, N. Bernier, R. Cipro, D. Lafond, G. Audoit, T. Baron, J. L. Rouviere, M. Martin, B. Chenevier, F. Bertin, Strain mapping at the nanoscale using precession electron diffraction in transmission electron microscope with off axis camera, Applied Physics Letters 105 (2014) 191906.

[29] C. Mahr, K. Müller-Caspary, T. Grieb, T. Mehrtens, M. Schowalter, F. F. Krause, D. Zillmann, A. Rosenauer, Theoretical study of precision and accuracy of strain analysis by nano-beam electron diffraction (SANBED), in: Microscopy Conference MC 2015, Göttingen (D), session MS 2, [Poster MS2.P023], 2015.

[30] R. Sellin, F. Heinrichsdorff, C. Ribbat, M. Grundmann, U. W. Pohl, D. Bimberg, Surface fattening during MOCVD of thin GaAs layers covering InGaAs quantum dots, Journal of Crystal Growth 221 (2000) 581–585.

[31] R. L. Sellin, C. Ribbat, M. Grundmann, N. N. Ledentsov, D. Bimberg, Cose-to-ideal device characteristics of high-power InGaAs/GaAs quantum dot lasers, Appl. Phys. Lett. 78 (2001) 1207.

[32] J. Scott, F. T. Docherty, M. MacKenzie, W. Smith, B. Miller, C. L. Collins, A. J. Craven, Sample preparation for nanoanalytical electron microscopy using the FIB lift-out method and low energy ion milling, J. Phys.: Conf. Ser. 26 (2006) 223–226.

[33] T. Mehrtens, S. Bley, P. V. Satyam, A. Rosenauer, Optimization of the preparation of GaN-based specimens with low-energy ion milling for (S)TEM, Micron 43 (2012) 902 – 909.

[34] J. M. LeBeau, S. D. Findlay, L. J. Allen, S. Stemmer, Position averaged convergent beam electron diffraction: Theory and applications, Ultramicroscopy 110 (2010) 118 – 125.

[35] A. Weickenmeier, H. Kohl, Computation of absorptive form factors for high-energy electron diffraction, Acta Crystallographica Section A 47 (1991) 590–597.

[36] K. Ishizuka, A practical approach for STEM image simulation based on the FFT multislice method, Ultramicroscopy 90 (2002) 71.

[37] A. Rosenauer, M. Schowalter, STEMSIM-a new software tool for simulation of STEM HAADF Z-contrast imaging, in: A. G. Cullis, P. A. Midgley (Eds.), Springer Proceedings in Physics, volume 120, Springer, 2007, pp. 169–172.

[38] S. Plimpton, Fast Parallel Algorithms for Short-Range Molecular Dynamics, Journal of Computational Physics 117 (1995) 1 – 19.

[39] M. Schowalter, K. Müller, A. Rosenauer, Scattering amplitudes and static atomic correction factors for the compositio n-sensitive 002 reflection in sphalerite ternary III–V and II–VI semiconductors, Acta Crystallographica Section A 68 (2012) 68–76.

[40] V. Grillo, E. Carlino, F. Glas, Influence of the static atomic displacement on atomic resolution Z-contrast imaging, Phys. Rev. B 77 (2008) 054103.

[41] F. Glas, The effect of the static atomic displacements on the structure factors of weak reflections in cubic semiconductor alloys, Phil. Mag. 84 (2004) 2055.

[42] K. Müller, M. Schowalter, A. Rosenauer, O. Rubel, K. Volz, Effect of bonding and static atomic displacements on composition quantification in $In_xGa_{1-x}N_yAs_{1-y}$, Phys. Rev. B 81 (2010) 075315.

[43] V. Grillo, K. Müller, K. Volz, F. Glas, T. Grieb, A. Rosenauer, Strain, composition and disorder in ADF imaging of semiconductors, Journal of Physics: Conference Series 326 (2011) 012006.

[44] V. Grillo, The effect of surface strain relaxation on HAADF imaging, Ultramicroscopy 109 (2009) 1453 – 1464.

ACCEPTED MANUSCRIPT

[45] T. Grieb, K. Müller, R. Fritz, V. Grillo, M. Schowalter, K. Volz, A. Rosenauer, Quantitative chemical evaluation of dilute GaNAs using ADF STEM: Avoiding surface strain induced artifacts, Ultramicroscopy 129 (2013) 1–9.
[46] T. Grieb, F. F. Krause, C. Mahr, D. Zillmann, K. Müller-Caspary, M. Schowalter, A. Rosenauer, Optimization of NBED simulations for disc-detection measurements, Ultramicroscopy 181 (2017) 50 – 60.
[47] A. Thust, High-Resolution Transmission Electron Microscopy on an Absolute Contrast Scale, Physical Review Letters 102 (2009) 220801.
[48] F. F. Krause, K. Müller, D. Zillmann, J. Jansen, M. Schowalter, A. Rosenauer, Comparison of intensity and absolute contrast of simulated and experimental high-resolution transmission electron microscopy images for different multislice simulation methods, Ultramicroscopy 134 (2013) 94–101.
[49] D. Cooper, A. Béché, J. M. Hartmann, L. Hutin, C. Le Royer, J. L. Rouvière, Strain measurement for the semiconductor industry by dark field electron holography and nanobeam electron diffraction with nm-scale resolution, Semicond. Sci. Technol. 25 (2010) 095012.
[50] P. Favia, M. B. Gonzales, E. Simoen, P. Verheyen, D. Klenov, H. Bender, Nanobeam Diffraction: Technique Evaluation and Strain Measurement on Complementary Metal Oxide Semiconductor Devices, J. Electrochem. Soc. 158 (2011) H438–H446.
[51] D. Cooper, T. Denneulin, N. Bernier, A. Béché, J.-L. Rouvière, Strain mapping of semiconductor specimens with nm-scale resolution in a transmission electron microscope, Micron 80 (2016) 145–165.
[52] C. Mahr, K. Müller-Caspary, T. Grieb, F. F. Krause, M. Schowalter, A. Lackmann, A. Wittstock, A. Rosenauer, Measurement of local crystal lattice strain variations in dealloyed nanoporous gold, Mater. Res. Lett. 6 (2018) 84–92.
[53] J-L-Rouvière, Method to facilitate positioning of diffraction spots, Patent US 2013/9296968 A1 (2013).
[54] K. Müller-Caspary, F. F. Krause, T. Grieb, S. Löffler, M. Schowalter, A. Béché, V. Galioit, D. Marquardt, J. Zweck, P. Schattschneider, J. Verbeeck, A. Rosenauer, Measurement of atomic electric fields and charge densities from average momentum transfers using scanning transmission electron microscopy, Ultramicroscopy 178 (2017) 62–80.
[55] T. Mehrtens, K. Müller, M. Schowalter, D. Hu, D. M. Schaadt, A. Rosenauer, Measurement of indium concentration profiles and segregation efficiencies from high-angle annular dark field-scanning transmission electron microscopy images, Ultramicroscopy 131 (2013) 1–9.
[56] T. Grieb, K. Müller, E. Cadel, A. Beyer, M. Schowalter, E. Talbot, K. Volz, A. Rosenauer, Simultaneous Quantification of Indium and Nitrogen Concentration in InGaNAs Using HAADF-STEM, Microsc. Microanal. 20 (2014) 1740–1752.

ACCEPTED MANUSCRIPT